

Institute for Cross-Disciplinary Physics and
Complex



Simulation Methods

Non-classical Behaviour and Pattern Formation in DOPO

Author: Daniel Montesinos Capacete

January 30, 2024

Contents

1	Introducction	2
2	DOPO: Equations in Q-representation	2
3	Pattern Formation: Linear Stability	3
4	Numerical Solution	4
5	Results	5
5.1	Patterns for $L = 4\lambda_c$	5
5.2	Patterns for $L = 2.5\lambda_c$	7
6	Conclusion	10
A	Numerical Details	11
A.1	Generalized Stochastic Heun Method	11
A.2	Finite differences: Centered-Space Method	11
A.3	Centered-Space Heun Method	12
A.4	Code Implementation	13
A.5	Random Number Generator	13
B	Fourier Transform Details	13

1 Introduction

The Optical Parametric Oscillator (OPO) stands as a sophisticated device within the domain of nonlinear optics and laser technology. The OPO employs a nonlinear crystal in a cavity to convert a high intensity pump beam at frequency ω_1 , in two coherent beams at lower energies and distinct frequencies ω_2 and ω_3 [1]. The resulting frequencies are constrained to energy and momentum conservation. In the specific context of our study, we delve into the Degenerate Optical Parametric Oscillator (DOPO), where the frequencies of the two output beams are identical ($\omega_2 = \omega_3$). More precisely, we aim to study the pattern formation of the output beams in the DOPO around the threshold, taking into account quantum fluctuations represented as a noise term in the equations. In this regime, we will see a noisy precursor of the pattern, a phenomenon reflective of what can be characterized as a quantum image [2]. Thus, our aim is to reproduce the patterns that can be seen in [3] and understand how it changes when varying the system size.

2 DOPO: Equations in Q-representation

The behaviour of the pump beam and the degenerated output beams is studied by using two spatio-temporal fields $\hat{A}_0(\mathbf{x}, t)$, $\hat{A}_1(\mathbf{x}, t)$ representing the complex amplitude field of each beam respectively. Here, \mathbf{x} is the transverse coordinates to the propagation of the beams but we will restrict ourselves to study one single dimension so $\mathbf{x} = x$. The equations of the model are obtained by using the Q-representation on the Lindblad Master Equation. The set of equations that we get from this procedure is [3]

$$\begin{aligned}\partial_t \alpha_0(x, t) &= - \left[(1 + i\Delta_0) - i\partial_x^2 \right] \alpha_0(x, t) + E - \frac{1}{2} \alpha_1^2(x, t) + \sqrt{\frac{2}{d}} \frac{g}{\gamma} \xi_0(x, t), \\ \partial_t \alpha_1(x, t) &= - \left[(1 + i\Delta_1) - 2i\partial_x^2 \right] \alpha_1(x, t) + \alpha_0(x, t) \alpha_1^*(x, t) + \sqrt{\frac{2}{d}} \frac{g}{\gamma} \xi_1(x, t)\end{aligned}\tag{1}$$

where Δ_k represents the detuning of the beams, E is the intensity of the pump field, d and γ are constants that depend on the nonlinear medium, g relates to the strength of the interaction and $\xi_k(x, t)$ are the noises that represents quantum fluctuations. This set of stochastic differential equations has the same form in the Itô and Stratonovich interpretation as discussed in [3]. The complex amplitude fields $\alpha_k(x, t)$ are the Q-representation of the boson modes $\hat{A}_k(x, t)$. Remark that, in this set of equations, the time is given in units of γ [3]. The noise term $\xi_0(x, t)$ is a gaussian white noise

with variance one while $\xi_1(\mathbf{x}, t)$ is expressed as

$$\xi_1(x, t) = g_1(\alpha_0(\mathbf{x}, t))\phi(x, t) + g_2(\alpha_0(\mathbf{x}, t))\psi(x, t) \quad (2)$$

$$g_1(\alpha_0(\mathbf{x}, t)) = \frac{-\alpha_{0I}(x, t)}{2\sqrt{2 + \alpha_{0R}(x, t)}} + \frac{i}{2}\sqrt{2 + \alpha_{0R}(x, t)} \quad (3)$$

$$g_2(\alpha_0(\mathbf{x}, t)) = \sqrt{\frac{1 - \frac{|\alpha_0(x, t)|^2}{4}}{2 + \alpha_{0R}(x, t)}} \quad (4)$$

where $\alpha_0(\mathbf{x}, t) = \alpha_{0R}(\mathbf{x}, t) + i\alpha_{0I}(\mathbf{x}, t)$ and $\phi(x, t)$, $\psi(x, t)$ are uncorrelated gaussian white noises. In order to derive the equations for the numerical approach, expressing them in a more concise form is advantageous and leads to

$$\partial_t \alpha_k(\mathbf{x}, t) = -[z_k - a_k i \partial_x^2] \alpha_k(\mathbf{x}, t) + f_k(\alpha_0(\mathbf{x}, t), \alpha_1(\mathbf{x}, t), E) + b_k \xi_k(\mathbf{x}, t) \quad (5)$$

for $k = 0, 1$ and the value of the different terms is given by

$$z_k = 1 + i\Delta_k, \quad a_0 = 1, \quad a_1 = 2, \quad b_k = \sqrt{\frac{2}{d}} \frac{g}{\gamma}, \quad k = 0, 1 \quad (6)$$

$$f_0(\alpha_1(\mathbf{x}, t), E) = E - \frac{1}{2}\alpha_1^2(\mathbf{x}, t), \quad f_1(\alpha_0(\mathbf{x}, t), \alpha_1(\mathbf{x}, t)) = \alpha_0(\mathbf{x}, t)\alpha_1^*(\mathbf{x}, t).$$

Examining Eq. (5), we can see that the term associated with z_k relates to losses within the optical medium, while the component originating from the Laplacian represents the diffraction term. The nonlinear functions $f_k(\alpha_0(\mathbf{x}, t), \alpha_1(\mathbf{x}, t), E)$ emerge from the nonlinear characteristics of the medium, and the noises $\xi_k(\mathbf{x}, t)$ model quantum fluctuations.

3 Pattern Formation: Linear Stability

We aim to show how a stripe pattern appears in the simulations as we increase the intensity of the pump field E above threshold. From Eq. (1), focusing on the classical equation (ignoring the noise term), a steady and homogeneous solution can be easily obtained

$$\alpha_0^{st} = \frac{E}{1 + i\Delta_0}, \quad \alpha_1^{st} = 0. \quad (7)$$

Performing a linear stability around this solution gives the following dispersion relation for the growth of perturbations with wave vector k [3]

$$\lambda_{\pm}(k) = -1 \pm \sqrt{|\alpha_0^{st}| - (\Delta_1 + 2k^2)^2}. \quad (8)$$

The unstable modes will be given by $\lambda_+(k)$ since $\lambda_-(k) < 0$. The homogeneous and steady solution becomes unstable at $E_c = \sqrt{1 + \Delta_0^2}$ with a critical value for the wave number $|k_c| = \sqrt{-\Delta_1/2}$. We will use this dispersion relation to understand the results from the simulations.

4 Numerical Solution

In here, we present the equations for the numerical integration to solve Ec. (5). We are addressing a problem involving a system of two coupled partial stochastic nonlinear differential equations in complex variable. In order to to that, we will use the centered-space Heun method. Since the equations we are dealing with are not in the standard form that we have seen in the lectures, it is needed to adapt the methods for this case. This is done in detail in Appendix A. After doing this procedure, it can be seen that the equations for the numerical integration of Eq. (5) are given by

$$\begin{aligned}
A_{k,n}^{(1)}(t_j) &= A_{k,n}(t_j) + \Delta t [-z_k A_{k,n}(t_j) + D_k \delta A_{k,n}(t_j) + f_k] + b_k \sqrt{\frac{\Delta t}{\Delta x}} w_{k,n}(t_j) \\
A_{k,n}(t_{j+1}) &= A_{k,n}(t_j) - \frac{\Delta t z_k}{2} (A_{k,n}(t_j) + A_{k,n}^{(1)}(t_j)) + \frac{\Delta t D_k}{2} (\delta A_{k,n}(t_j) + \delta A_{k,n}^{(1)}(t_j)) \\
&\quad + \frac{\Delta t}{2} (f_k(A_{0,n}(t_j), E) + f_k(A_{0,n}^{(1)}(t_j), E)) + \frac{1}{2} b_k \sqrt{\frac{\Delta t}{\Delta x}} (w_{k,n}(t_j) + w_{k,n}^{(1)}(t_j))
\end{aligned} \tag{9}$$

where $A_{k,n}(t_j)$ relates to the field $\alpha_k(x, t)$ after doing the coarse graining. We are going to use periodic boundary conditions for both fields. The rest of the terms are defined as

$$\begin{aligned}
D_k &\equiv i \frac{a_k}{(\Delta x)^2}, \quad w_{0,n}(t_j) = w_{0,n}^{(1)}(t_j) \equiv u_n(t_j), \quad w_{1,n}(t_j) \equiv \sum_{l=1}^2 u_{l,n}(t_j) g_l(A_{0,n}(t_j)), \\
w_{1,n}^{(1)}(t_j) &\equiv \sum_{l=1}^2 u_{l,n}(t_j) g_l(A_{0,n}^{(1)}(t_j)), \quad \delta A_{k,n}(t_j) \equiv A_{k,n+1}(t_j) - 2A_{k,n}(t_j) + A_{k,n-1}(t_j)
\end{aligned} \tag{10}$$

where $u_n(t_j)$ and $u_{l,n}(t_j)$ are independent gaussian random numbers with zero mean and variance one.

The values for the parameters of the model that we are going to use are the same as in [3]. Thus, we will work with

$$\Delta_0 = 0, \quad \Delta_1 = -0.18, \quad \frac{g}{\sqrt{d}\gamma} = 10^{-4} \tag{11}$$

which leads to $E_c = 1.0$ and $|k_c| = 0.3$. Thus, we expect to find stripe patterns for values of $E \geq 1$. The time discretization will be fixed to $\Delta t = 0.01$ while for the space discretization we will use two different values depending on system size. In order to show how we can miss the critical wave number by choosing a wrong space discretization, we will be using a fixed number of points $n = 64$. Thus, the time discretization will be given by $\Delta x = L/(n - 1)$ where L is the system size. In what follows, we will be discussing results for $L = 4\lambda_c$ and $L = 2.5\lambda_c$ where $\lambda_c = 2\pi/|k_c|$. Note that the Courant criterion for the stability of the numerical solution are satisfied with both $\Delta x \approx 1.33$ ($L = 4\lambda_c$) and $\Delta x \approx 0.83$ ($L = 2.5\lambda_c$)

$$\frac{2a_0\Delta t}{(\Delta x)^2} < 1, \quad \frac{2a_1\Delta t}{(\Delta x)^2} < 1. \quad (12)$$

5 Results

In each of the simulations, we will start with the following initial conditions:

$$A_{0,n}(0) = E \quad \forall n, \quad A_{1,n}(0) = 10^{-5}(\epsilon(x_n) + 10\sin(k_c x_n)) \quad (13)$$

where $\epsilon(x_n)$ is a gaussian random number of variance one and zero mean and x_n relates to the discrete position. This initial conditions are the same as in [3]. We will take measures every 10^5 time steps and the results will show a total of 200 measurements.

5.1 Patterns for $L = 4\lambda_c$

This case correspond to the system size that is used in [3]. Thus, in this section we aim to reproduce the patterns and see how it changes when moving slightly above threshold. The temporal evolution of the real part of $\alpha_1(x, t)$ and the module square of its Fourier transform are shown in Fig. 1 for four different values of E . The white and black colors correspond to maxima and minima respectively. It is observed that, as we increase the value of E above threshold, we find that there is a stripe pattern with wave number $k_c = 0.3$ as expected by the linear stability analysis. The value of the wave number is obtained looking at the maximums of the Fourier transform on each of the plots. Apart from this maximum value, the Fourier transform shows strong fluctuations on the background due to the noise.

The in-homogeneous field that we see for $E = 0.999$ is the quantum image which is purely produced by the noise term representing quantum fluctuations. This phenomenon is known as the noisy precursor, where we observe the incipient emergence of the stripe pattern, although it has not reached full formation. For this value of the

pump field, we would expect an homogeneous solution in the classical equations since all the modes have a negative dispersion relation. For $E = 1.0$, we observe that the pattern is not yet fully present, but the system begins to exhibit some pattern-like structure as we approach the threshold. By slightly increasing the intensity of the pump field to $E = 1.001$, the pattern becomes fully formed, revealing four complete wavelengths due to our system size of $L = 4\lambda_c$. For $E = 1.005$, we can see that a second maximum appears for $k = 0.9$. This maximum correspond to the third harmonic of the k_c mode which has a wave number $k = 3k_c$ [4]. Harmonics emerge due to nonlinear interactions in the system and their amplitude is increased as we move farther away from the threshold. To understand the specific behaviour of the harmonics, a non linear analysis of Ec. (1) is needed but this is out of the scope of this study.

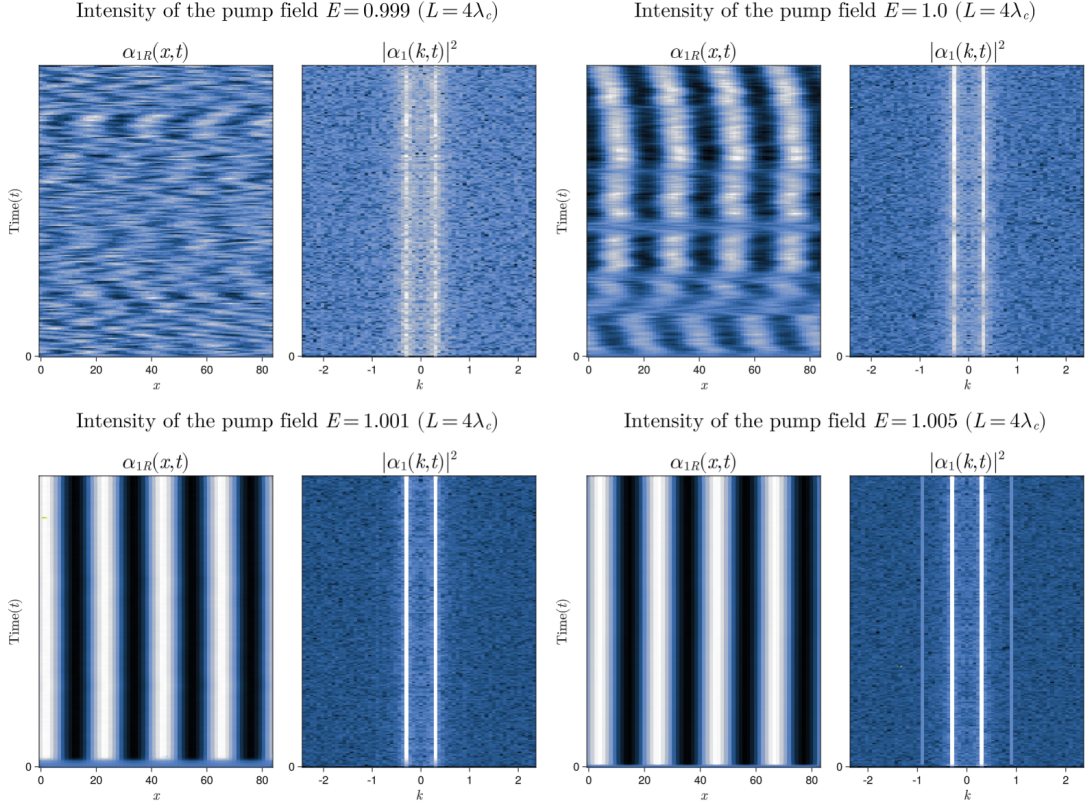


Figure 1: For each of the four plots, on the left side the real part of $\alpha_1(x, t)$ is plotted while on the right side the module square of its Fourier transform is shown. The value for the right side are in log-scale and the vertical axis represents the time while horizontal axis is the x position or its corresponding wave number k . It can be seen how a stripe patterns appear above threshold ($E_c = 1.0$).

On the other hand, the results for the same values of E but zero noise ($b_k = 0$) are shown in Fig. 2. In these pictures we can see that the field is homogeneous for $E = 0.999$ as we would expect since all the modes are stable. Even though there is no pattern, we can see some peaks for k that are related to the initial condition. Above threshold, the same patterns as before are obtained. It is interesting to note that the Fourier transform does not have any fluctuations since we are not including the noise term.

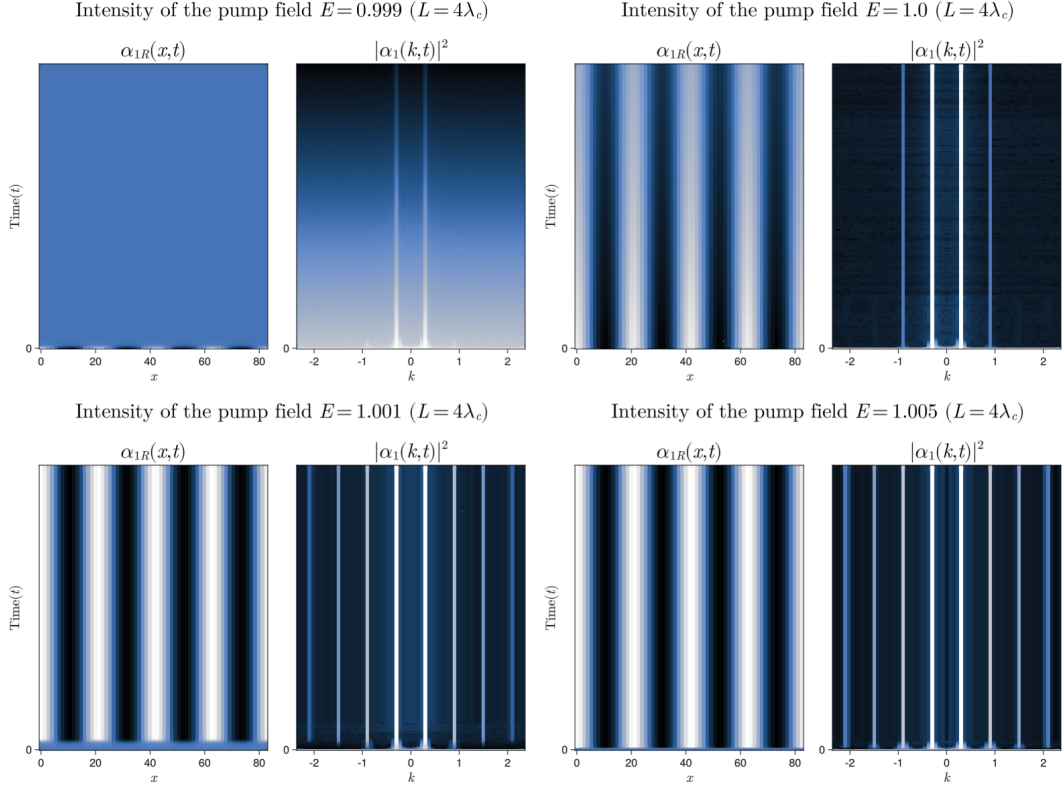


Figure 2: This case correspond to $b_k = 0$ (turning off the noise). For each of the four plots, on the left side the real part of $\alpha_1(x,t)$ is plotted while on the right side the module square of its Fourier transform is shown. The value for the right side are in log-scale and the vertical axis represents the time while horizontal axis is the x position or its corresponding wave number k .

5.2 Patterns for $L = 2.5\lambda_c$

In this section, our aim is to illustrate and understand how the threshold can change for a different system size while maintaining a fixed number of $n = 64$ points. This

will change the space discretization as we have discussed in Sec. 4.

The results for this case are shown in Fig. 3. We can observe how the stripe pattern does not appear when we immediately go above $E = 1.0$. For, $E = 1.001$, the behaviour is essentially the same as for $E = 0.999$ and we do not see any pattern. However, the pattern still appears for $E = 1.005$ with the maximum of the wave number for $k'_c \approx 0.24$ and its third harmonic $k = 3k'_c$. Note that in this case we can only see two wave lengths in the pattern due to the value of the system size.

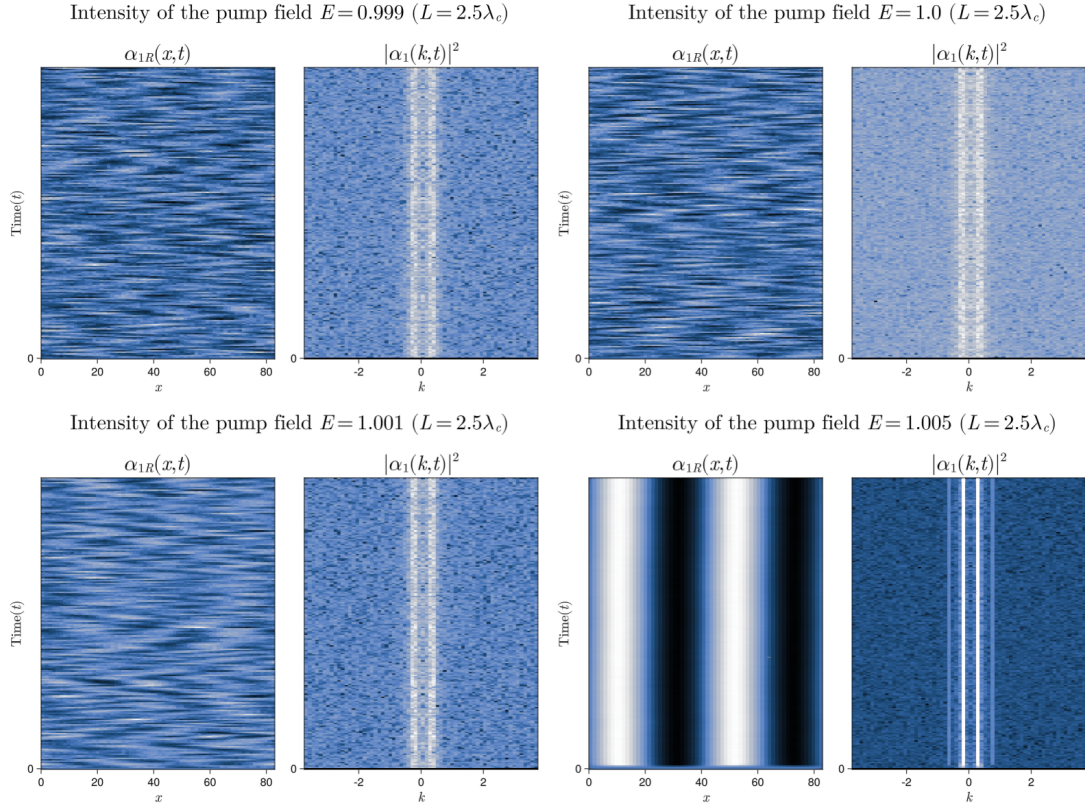


Figure 3: For each of the four plots, on the left side the real part of $\alpha_1(x, t)$ is plotted while on the right side the module square of its Fourier transform is shown. The value for the right side are in log-scale and the vertical axis represents the time while horizontal axis is the x position or its corresponding wave number k .

In order explain the results shown in Fig. 3 and understand the reasons for the pattern to not appear immediately above $E = 1.0$, we need to look at the dispersion relation $\lambda_+(k)$ given by Ec. (8). In Fig. 4, $\lambda_+(k)$ is shown for various values of E . Along with it, the red and green dots represent the k values corresponding to the

space discretization for $L = 4\lambda_c$ and $L = 2.5\lambda_c$ respectively. Looking at this figure, we see how the discretization for $L = 2.5\lambda_c$ misses the critical wave number $|k_c| = 0.3$ (See Ap. B for details on how the discretization for k is obtained). Thus, we can see that, even when we are using $E = 1.001$, none of the modes that are involved in this discretization have a positive value of the dispersion. This explains the behaviour of the pattern for $L = 2.5\lambda_c$. Increasing the value of the intensity up to $E = 1.005$, is enough for the modes to have a positive value of the dispersion and recover the same stripe pattern that we have for $L = 4.0\lambda_c$ but for a slightly different value of $k'_c \approx 0.24$.

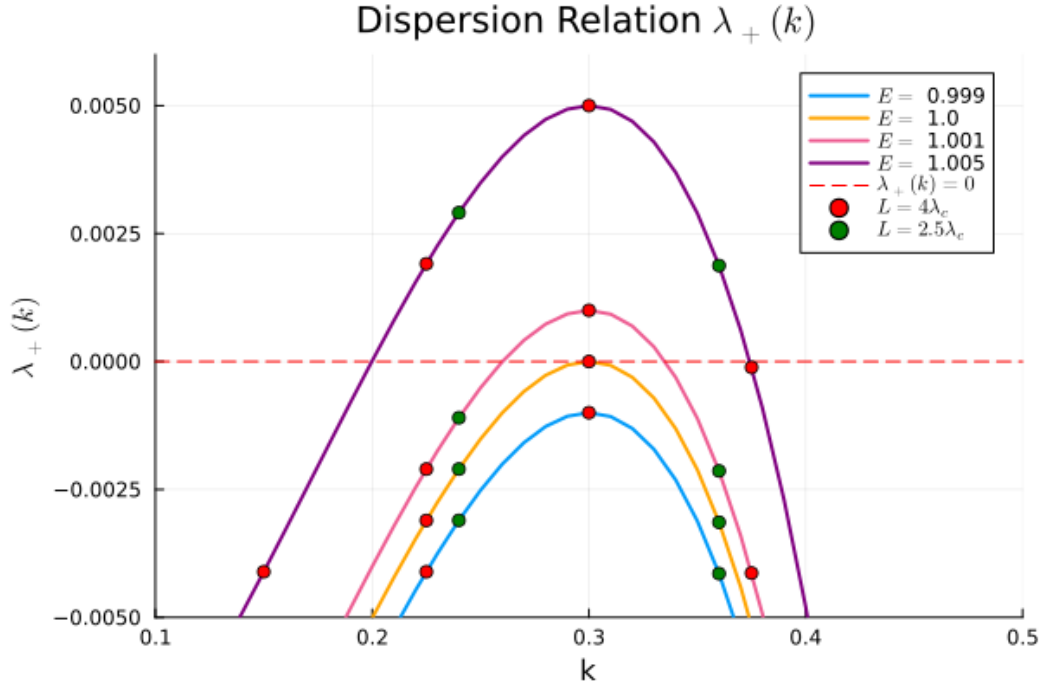


Figure 4: Dispersion relation obtained by linear stability analysis of Eq. (1) for several values of E . The points correspond to the discretization depending on the value of the system size L .

Note that, for a big enough value of E , there are more than one mode with positive dispersion relation but in the pattern we only see the maxima corresponding to the critical wave length and its harmonics. For example, this happens for $E = 1.005$ as can be seen in Fig. 4. These unstable modes are obtained by linear stability analysis, showcasing growth exclusively in the linear regime very close to the threshold. Upon entering the nonlinear regime with increased value of E , these modes engage in competitive dynamics, typically leading to the dominance of the most unstable one.

This prevailing mode establishes the final pattern with a distinct periodicity, while the other initially growing modes fade away during the nonlinear progression [4].

6 Conclusion

The numerical integration of the equations in the Q-representation for the DOPO given by Ec. (1) have been discussed. We have been able to reproduce the striped pattern that appears above threshold ($E_c = 1.0$) with the critical value of the wave number $|k_c| = 0.3$ as can be seen in Fig 1. This aligns with the prediction of linear stability analysis and the results are in accordance with [3]. Additionally, slightly under threshold, the noisy precursor of the pattern can be seen. This phenomenon is the quantum image produced by the fluctuations terms. In Fig. 2, it is possible to see that the noisy precursor does not appear as we turn off the noise. This is done for a system size of $L = 4\lambda_c$.

Apart from that, we have also shown that the threshold can change due to the finite size of the system. This is shown in Fig. 3 in which the pattern appears for $E = 1.005$ instead of $E_c = 1.0$. This behaviour is understood in terms of the dispersion relation and the discretized values of k that we are using as illustrated in Fig. 4.

A Numerical Details

A.1 Generalized Stochastic Heun Method

For solving the second equation of the system given by Eq. (5), we need to deal with two uncorrelated noises in the same equation. Thus, we will briefly discuss how to apply the Heun method for an equation with d uncorrelated gaussian white noises $\xi_j(t)$. The general equation we aim to solve is

$$\frac{dx}{dt} = q(x(t), t) + \sum_{j=1}^d g_j(x(t), t) \xi_j(t) \quad (14)$$

Applying the same procedure that we did in the lectures, we get

$$\begin{aligned} x^{(1)}(t_i) &= x(t_i) + \Delta t q(x(t_i), t_i) + \Delta t \sum_{j=1}^d u_j(t_i) g_j(x(t_i), t_i) \\ x(t_{i+1}) &= x(t_i) + \frac{\Delta t}{2} \left[q(x(t_i), t_i) + q(x^{(1)}(t_i), t_{i+1}) \right] \\ &\quad + \frac{\sqrt{\Delta t}}{2} \sum_{j=1}^d u_j(t_i) \left[g_j(x(t_i), t_i) + g_j(x^{(1)}(t_i), t_{i+1}) \right] \end{aligned} \quad (15)$$

where $u_j(t_i)$ are independent gaussian random numbers with zero mean and variance one.

A.2 Finite differences: Centered-Space Method

To solve Eq. (5) using finite differences, it is necessary to employ coarse graining to address the noise as follows

$$A_{k,n}(t) = \frac{1}{\sqrt{\Delta x}} \int_{x_n}^{x_{n+1}} \alpha_k(x, t) dx, \quad \xi_{k,n}^{cg}(t) = \frac{1}{\sqrt{\Delta x}} \int_{x_n}^{x_{n+1}} \xi_k(x, t) dx. \quad (16)$$

Therefore, employing the centered space method, where the second spatial derivative is expressed as

$$\left. \frac{\partial^2 \alpha_k(x, t)}{\partial x^2} \right|_{x_n, t_j} \Rightarrow \frac{A_{k,n+1}(t_i) - 2A_{k,n}(t_i) + A_{k,n-1}(t_i)}{(\Delta x)^2} + \mathcal{O}[(\Delta x)^3] \quad (17)$$

we find that Eq. (5) is transformed to

$$\begin{aligned} \frac{dA_{k,n}(t)}{dt} &= -z_k A_{k,n}(t) + a_k i \left[\frac{A_{k,n+1}(t_i) - 2A_{k,n}(t_i) + A_{k,n-1}(t_i)}{(\Delta x)^2} \right] \\ &\quad + f_k(A_{k,0}(t), A_{k,1}(t), t, E) + \frac{b_k}{\sqrt{\Delta x}} \xi_{k,n}(t) \end{aligned} \quad (18)$$

and the corresponding functions:

$$\begin{aligned} f_0(A_{0,n}(t), E) &= E - \frac{1}{2}A_{1,n}(t)^2 \\ f_1(A_{0,n}(t), A_{1,n}(t)) &= A_{0,n}(t)A_{1,n}^*(t) \end{aligned} \quad (19)$$

A.3 Centered-Space Heun Method

Finally, by applying the Heun method that we have shown in appendix A.1 to Eq. (18), we obtain the equations for the numerical integration of Eq. (5). In order to write these expressions concisely, we define

$$\delta A_{k,n}(t_i) \equiv A_{k,n+1}(t_i) - 2A_{k,n}(t_i) + A_{k,n-1}(t_i). \quad (20)$$

Thus, for $A_{0,n}(t)$ we obtain

$$\begin{aligned} A_{0,n}^{(1)}(t_j) &= A_{0,n}(t_j) + \Delta t \left[-z_0 A_{0,n}(t_j) + i \frac{a_0}{(\Delta x)^2} \delta A_{0,n}(t_j) + f_0(A_{0,n}(t_j), E) \right] + b_0 \sqrt{\frac{\Delta t}{\Delta x}} u_n(t_j), \\ A_{0,n}(t_{j+1}) &= A_{0,n}(t_j) - \frac{\Delta t z_0}{2} \left(A_{0,n}(t_j) + A_{0,n}^{(1)}(t_j) \right) + i \frac{a_0 \Delta t}{2(\Delta x)^2} \left(\delta A_{0,n}(t_j) + \delta A_{0,n}^{(1)}(t_j) \right) \\ &\quad + \frac{\Delta t}{2} \left(f_0(A_{0,n}(t_j), E) + f_0(A_{0,n}^{(1)}(t_j), E) \right) + b_0 \sqrt{\frac{\Delta t}{\Delta x}} u_n(t_j) \end{aligned} \quad (21)$$

and for $A_{1,n}(t)$ the result is

$$\begin{aligned} A_{1,n}^{(1)}(t_j) &= A_{1,n}(t_j) + \Delta t \left[-z_1 A_{1,n}(t_j) + i \frac{a_1}{(\Delta x)^2} \delta A_{1,n}(t_j) + f_1(A_{0,n}(t_j), E) \right] \\ &\quad + b_1 \sqrt{\frac{\Delta t}{\Delta x}} \left(g_1(A_{0,n}(t_j)) u_{1,n}(t_j) + g_2(A_{0,n}(t_j)) u_{2,n}(t_j) \right), \\ A_{1,n}(t_{j+1}) &= A_{1,n}(t_j) - \frac{\Delta t z_1}{2} \left(A_{1,n}(t_j) + A_{1,n}^{(1)}(t_{j+1}) \right) + i \frac{a_1 \Delta t}{2(\Delta x)^2} \left(\delta A_{1,n}(t_j) + \delta A_{1,n}^{(1)}(t_j) \right) \\ &\quad + \frac{\Delta t}{2} \left(f_1(A_{0,n}(t_j), A_{1,n}(t_j)) + f_1(A_{0,n}^{(1)}(t_j), A_{1,n}^{(1)}(t_j), E) \right) \\ &\quad + \frac{1}{2} \sqrt{\frac{\Delta t}{\Delta x}} b_1 \sum_{l=1}^2 u_{l,n}(t_j) \left(g_l(A_{0,n}(t_j)) + g_l(A_{0,n}^{(1)}(t_j)) \right). \end{aligned} \quad (22)$$

These equations are written in a compact form in Eq. (9).

A.4 Code Implementation

Even though it would be enough to work directly with Eq. (21) and Eq. (22), it is convenient to simplify these expressions and write them in a compact form in order to have a clean implementation in the code. Looking at Eq. (9), the equations for the numerical integration of Eq. (5) can be written as

$$\begin{aligned}
\lambda_{k,n}(t_j) &= \Delta t \left[-z_k A_{k,n}(t_j) + i \frac{a_k}{(\Delta x)^2} \delta A_{k,n}(t_j) + f_k(A_{0,n}(t_j), A_{1,n}(t_j), E) \right] + b_k \sqrt{\frac{\Delta t}{\Delta x}} w_{k,n}, \\
A_{k,n}^{(1)}(t_j) &= A_{k,n}(t_j) + \lambda_{k,n}(t_j), \\
A_{k,n}(t_{j+1}) &= A_{k,n}(t_j) + \frac{1}{2} \lambda_k + \frac{\Delta t}{2} \left(-z_k A_{1,n}^{(1)}(t_j) + D_k \delta A_{1,n}^{(1)}(t_j) + f_k(A_{0,n}^{(1)}(t_i), A_{1,n}^{(1)}(t_i), E) \right) \\
&\quad + \frac{1}{2} b_k \sqrt{\frac{\Delta t}{\Delta x}} w_{k,n}^{(1)}
\end{aligned} \tag{23}$$

for $k = 0, 1$. These are the equations that we will use in the code. In order to do so, we will use Julia as our programming language. Using Julia, we can directly work with complex number so there is no need to separate the real and imaginary part in different equations.

A.5 Random Number Generator

All computations in this study will be conducted using the Julia programming language, employing its default random number generator, the Xoshiro256++ algorithm [5].

B Fourier Transform Details

In order to perform the Fourier transform of the field $\alpha_1(x, t)$, the FFTW.jl Julia package have been used [6]. Using this package, the discrete values of the wave length for a given system size L and a fixed number of points $n = 64$ are computed following

$$k_m = \frac{2\pi}{L} m, \quad m = 1 - \frac{n}{2}, \dots, \frac{n}{2} - 1. \tag{24}$$

Thus, when changing the value of L , we get a different value of the discretization in k leading to the results that are discussed in this study.

References

- [1] M.H. Dunn and Majid Ebrahim-Zadeh. “Optical parametric oscillators”. In: *Optics IV* (2000), pp. 61–82. DOI: <https://doi.org/10.1364/ASSP.2009.TuC1>.
- [2] Christophe Szwaj et al. “Quantum images in non degenerate optical parametric oscillators”. In: *The European Physical Journal D* 10 (2000), pp. 433–448. DOI: [10.1007/s100530050566](https://doi.org/10.1007/s100530050566).
- [3] Roberta Zambrini et al. “Non-classical behavior in multimode and disordered transverse structures in OPO: Use of the Q-representation”. In: *Springer* 22 (2003), pp. 461–471. DOI: <https://doi.org/10.1140/epjd/e2003-00019-7>.
- [4] Michael Cross and Henry Greenside. “Nonlinear states”. In: *Pattern Formation and Dynamics in Nonequilibrium Systems*. Cambridge University Press, 2009, pp. 126–172. DOI: [10.1017/CB09780511627200.005](https://doi.org/10.1017/CB09780511627200.005).
- [5] Jeff Bezanson et al. “Julia: A fresh approach to numerical computing”. In: *SIAM review* 59.1 (2017), pp. 65–98. DOI: <https://doi.org/10.1137/141000671>.
- [6] Matteo Frigo and Steven G. Johnson. “The Design and Implementation of FFTW3”. In: *Proceedings of the IEEE* 93.2 (2005). Special issue on “Program Generation, Optimization, and Platform Adaptation”, pp. 216–231. DOI: [10.1109/JPROC.2004.840301](https://doi.org/10.1109/JPROC.2004.840301).